COMMUNICATIONS IN SCIENCE AND TECHNOLOGY
Homepage: cst.kipmi.or.id

Preparation of Mo-impregnated mordenite catalysts for the conversion of refined kernel palm oil into bioavtur

Wega Trisunaryanti[a,*], Triyono[a], Karna Wijaya[a], Indriana Kartini[a], Suryo Purwono[b], Rodiansono[c], Ady Mara[d], Amsal Budiansyah[a]

[a]*Department of Chemistry, Universitas Gadjah Mada, Yogyakarta 55281, Indonesia*
[b]*Department of Chemical Engineering, Universitas Gadjah Mada, Yogyakarta 55281, Indonesia*
[c]*Department of Chemistry, Universitas Lambung Mangkurat, Banjarmasin 7071, Indonesia*
[d]*Department of Chemistry, Universitas Sriwijaya, Palembang 30862, Indonesia*

Article history:
Received: 2 October 2023 / Received in revised form: 20 December 2023 / Accepted: 20 December 2023

Abstract

The research aims to study the effects of Mo metal embedded on H-Mordenite on its activity and selectivity of hydrodeoxygenation (HDO) for Refined Palm Kernel Oil (RPKO) into bioavtur. The RPKO was obtained from the results of degumming and bleaching process of palm kernel oil and then analyzed using Gas Chromatography-Mass Spectrometer (GC-MS). The impregnation of Mo metal was carried out by spraying using an ammonium heptamolybdate precursor solution ($(NH_4)_6Mo_7O_{24}$•$4H_2O$) with an initial Mo metal content of 5, 10, and 15wt% of H-Mordenite to produce 5-Mo/Mor, 10-Mo/Mor, and 15-Mo/Mor. The 15-Mo/Mor catalyst produced the highest amount of liquid product (46.08wt%) with bioavtur yield of 43.19wt%. The usability test showed that 15-Mo/Mor catalyst still produced a good performance after three times of use in the RPKO feed HDO with the second and third run test liquid product of 34.82 and 46.14wt% respectively with bioavtur yield of 32.58 and 43.45wt%, respectively.

Keywords: Bioavtur; H-mordenite; hydrodeoxygenation; molybdenum; palm kernel oil

1. Introduction

The increasing aircraft usage will lead to the increasing aviation fuel consumption. The use of avtur as an aircraft fuel is a challenge for the energy sector because it is a fossil fuel. Fossil fuels contribute to global warming, which is a major problem in various parts of the world. Many countries plan to reduce carbon dioxide gas emissions towards a carbon neutral country by 2030 [1-3].

Vegetable oil such as palm kernel oil (PKO) can be used as an alternative raw material to replace petroleum in producing fuel oil, aviation fuel, diesel fuel and more [4-8]. It consists of saturated and unsaturated fatty acid chains, which are potential to be converted into other product forms such as alkanes, alkenes, or aromatics, dependent upon the catalyst and reaction conditions used [9-10]. PKO also contains 85% saturated fatty acid (SFA), mainly lauric acid (47.8%), and myristic acid (16.3%) [11].

The use of bioavtur can also reduce the greenhouse gas effect on the aviation life cycle to around 68.1% by 2050 [12]. The conversion of refined palm kernel oil (RPKO) into bioavtur can be done with the hydrodeoxygenation (HDO) process. Hydrodeoxygenation is an energy-efficient method to reduce the oxygen content in bio-oil [13-15]. This process uses a catalyst to increase the reaction rate resulting HDO as the main reaction to produce bioavtur.

To maximize HDO reaction frequency, the selected catalyst needs to be able to act as Brønsted acid sites, which are very influential in HDO reactions in view of the ability to bind hydrogen and release it to bind with the hydrodeoxygenated vegetable oil [9, 16]. Mo metal has a role in deoxygenation reactions for acting as a Brønsted acid side that can activate C-O [17-18]. Mo metal can also be used for catalytic processes as it has a single electron *d* orbital functioning as a Brønsted acid as a hydrogen breaker (homolytic) and an empty *p* orbital as Lewis acid, which binds the hydrogen [19]. For having a half-full *d* orbital, Mo metal is a metal that has stable electrons. Bioavtur has a hydrocarbon fraction from cracking vegetable oil with a chain length between C_8 and C_{16} [20].

Spray-dry impregnation is a technique for impregnating metals to the catalyst surface by spraying a precursor solution onto the support [21]. Spray-dry impregnation is widely applied on a large industrial scale considering it more advantageous than other methods. The spray method can control the formation of uniform small particles and distribute them evenly to the catalyst surface; this method can also reduce the use of solvents and the drying time of the catalyst.

Several studies on the conversion of vegetable oils into bioavtur have been conducted. One of the studies is the synthesis of bioavtur from coconut oil using a NiO/Silica-rich zeolite catalyst [22]. Last year, a study by Ibrahim et al.

* Corresponding author. Tel.: +62 811-256-055.
Email: wegats@ugm.ac.id
https://doi.org/10.21924/cst.8.2.2023.1288

produced biofuels from Malapari oil using Parangtritis beach sand that was wet impregnated by nickel as the catalyst that produced 33.61wt% bioavtur [23]. Wet impregnation is simpler to do, but it uses many amounts of solvents, risking the metals still in the solvents, not on the support. Compared to previous research, the novelty in this study is on the use of H-mordenite as a catalyst support with distributed molybdenum (Mo) metal catalyst by dry impregnation method using less solvent, leading it to be more efficient and economical compared to wet impregnation. Although metal Mo has been widely used as a metal catalyst, but there has been no research for the synthesis of bioavtur with monometal catalyst, H-mordenite as support, using dry impregnation method.

2. Materials and Methods

2.1. Materials

Materials used for the research included Palm Kernel Oil (PKO) from PT Sinar Mas Agro Resources (Indonesia), H-Mordenite, ammonium heptamolybdate tetrahydrate ($(NH_4)_6Mo_7O_{24}•4H_2O$, Sigma-Aldrich (101182-250G)), Whatmann paper No. 42. Phosphoric acid (H_3PO_4), bentonite and deionized water was produced from CV Bima Aksara Nusa. Nitrogen gas and hydrogen gas were produced from PT. Samator Gas. All chemicals and reagents were of analytical grade.

2.2. Instruments

The analytical instruments used were Fourier Transform Infrared Spectroscopy (FTIR, Shimadzu IR Prestige-21), X-Ray Diffraction (XRD, Shimadzu XRD-6000), Surface Area Analyzer (SAA, Quantachrome TouchWin v1.22), Scanning Electron Microscope-Energy Dispersive X-Ray (SEM-EDX, JEOL JED-2300), Temperature Programmed Desorption of Ammonia (NH_3-TPD, Micromeritrics Chemisorb 2750), and Gas Chromatography-Mass Spectrometer (GC-MS, Shimadzu QP2010S).

2.3. PKO Purification

Palm Kernel Oil (PKO) was purified through a degumming process inspired by the study of Nugraheni et al. [24]. 0.25 mL of Phosphoric acid for each 500 mL of PKO was bleached using bentonite as much as 3% of the PKO volume instead of activated carbon. It was then refluxed at 105°C for one hour. PKO feed that had been degummed and bleached was then centrifuged to separate the oil from impurities to obtain Refined Palm Kernel Oil (RPKO). RPKO was then analyzed and characterized using GC-MS.

2.4. Mo metal impregnation onto H-Mordenite

The impregnation of Mo metal into H-mordenite was carried out using dry impregnation method by spray inspired from Triyono et al. [25] with the difference of metal content distribution and precursor solution. The metal content of Mo metals distribution was made into 5, 10 and 15wt% respectively towards H-mordenite, resulting in each of samples named 5-Mo/Mor, 10-Mo/Mor, and 15-Mo/Mor. Dry impregnation method was done by spraying 9 mL of ammonium heptamolybdate precursor solution in a spray bottle for every 3 g of H-mordenite while stirring until it formed a paste. The Mo metal-embedded catalyst was dried using an oven for 2 h at 110°C. The dried catalyst was calcined using N_2 gas with a flow rate of 10 mL min^{-1} for 5 h at 500°C. Meanwhile, the reduction process was carried out using H_2 gas with a flow rate of 10 mL min^{-1} for 5 h at 500°C. The prepared catalysts were characterized using XRD, SAA, FTIR and SEM-EDX and tested for acidity using NH_3-TPD.

2.5. Hydrodeoxygenation of RPKO

The HDO process was done with a catalyst-to-feed ratio of 1:200 (w/v) using H_2 gas with a flow rate of 10 mL min^{-1} for 4 h in a semi-batch stainless steel reactor with double furnace in a one-pot system. Each obtained liquid product was then analyzed using GC-MS. Liquid products were collected at two temperature in the range of fraction I (400–500°C) to fraction II (500–600°C). The catalyst with the highest amount of liquid product was tested for usability three times.

The catalyst with the highest amount of liquid product was used for usability test by three times. The liquid product from each usability test run was analyzed by GC-MS, and the used catalyst was characterized by SEM-EDX. Products from HDO results were calculated using the following equations:

$$LP = \frac{W_{Product}}{W_{Feed}}\ x\ 100\% \quad (1)$$

$$S_B = \frac{A_B}{A_{Total}}\ x\ \frac{W_{Product}}{W_{Feed}}\ x\ 100\% \quad (2)$$

$$S_O = \frac{A_O}{A_T}\ x\ \frac{W_{Product}}{W_{Feed}}\ x\ 100\% \quad (3)$$

$$S_{Nb} = \frac{A_{Nb}}{A_T}\ x\ \frac{W_{Product}}{W_{Feed}}\ x\ 100\% \quad (4)$$

Description:

LP	= Liquid product conversion (wt%)
$W_{product}$	= Liquid product weight
W_{Feed}	= Feed weight
S_B	= Selectivity of bioavtur fraction (wt%)
A_T	= Total GC spectra area percentage (100%)
A_B	= GC spectra area of the bioavtur fraction (%)
S_O	= Selectivity of oxygenate compounds (wt%)
A_o	= GC spectra area of oxygenate compounds (%)
S_{Nb}	= Selectivity of non-bioavtur fraction (wt%)
A_{Nb}	= GC spectra area of the non-bioavtur fraction (%)

3. Results and Discussion

3.1. RPKO characterization

Table 1 shows the analysis of RPKO by GC-MS in which the results showed that PKO composition was similar with the one in the study by Mancini et al. [11] mostly containing lauric and myristic acid. The lauric and myristic acid carbon length are in the range with bioavtur, i.e. C_8 to C_{16} [20].

Table 1. RPKO compositions analysis by using GC-MS

Retention Time	Compound Name	Compound Formula	GC Area (%)
6.824	Caproic Acid	$C_6H_{12}O_2$	0.20
1.3674	Caprylic Acid	$C_7H_{14}O_2$	4.10
20.097	Capric Acid	$C_{10}H_{20}O_2$	4.08
25.772	Lauric Acid	$C_{12}O_{24}O_2$	54.70
30.689	Myristic Acid	$C_{14}H_{28}O_2$	16.27
35.147	Palmitic Acid	$C_{16}H_{32}O_2$	6.95
38.582	Hexadecane-9,12-dienic Acid	$C_{16}H_{30}O_2$	1.34
38.731	Oleic Acid	$C_{18}H_{34}O_2$	10.68
39.208	Stearic Acid	$C_{18}H_{38}O_2$	1.67

3.2. Catalyst functional groups analysis using FT-IR

The catalyst functional groups analysis result as shown in Figure 1 and Table 2 showed a specific absorption band at wave number 3425 cm^{-1}, which is predicted to be a stretching vibration of silanol groups (Si-O-H) and adsorbed water molecules (H-O-H). The presence of water molecules is emphasized at wave number 1640 cm^{-1}, which is a bending vibration of the H-O-H bond. The absorption band at wave numbers 420–500 cm^{-1} was the bending vibration of the Si–O/Al-O bond, wave number 870 cm^{-1} was the stretching vibration of the Mo-O-Mo bond, and the absorption band at wave number 575 cm^{-1} was the vibration of the Mo-O bond. In H-Mordenite, there was seemingly a Mo-O vibration, but it is not a Mo-O vibration where the FTIR did not detect that specific peak at 575 cm^{-1} but at 586.36 cm^{-1}.The appearance of Mo groups in the FT-IR spectra in each catalyst indicated that Mo has been successfully embedded on H-mordenite. The FT-IR spectra of the 15-Mo/Mor catalyst did not clearly show the vibration of silanol where the absorption band that appeared decreased in area and peak intensity. This might be determined by the block of Mo metal on the Si surface so that the vibrations of the silanol group could not be clearly seen in the spectra [29]. The 15-Mo/Mor catalyst lacking Mo-O-Mo bonding may be caused by the dry impregnation, which involved manual grinding and stirring. As a consequence, it did not result in the optimum results.

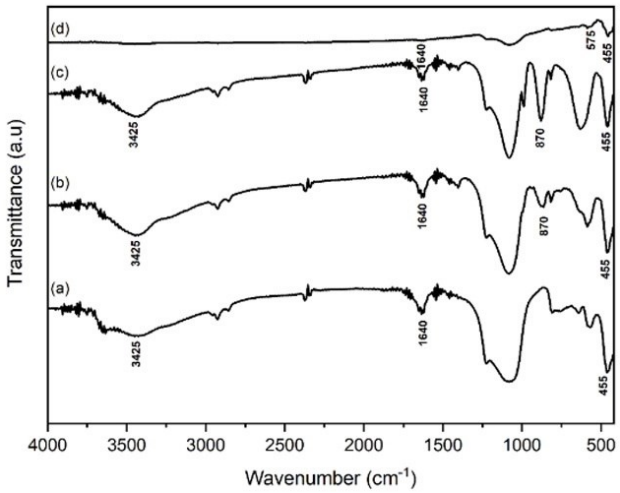

Fig. 1. FT-IR spectra of: (a) H-mordenite (b) 5-Mo/Mor; (c) 10-Mo/Mor; and (d) 15-Mo/Mor catalyst

Table 2. FT-IR spectra interpretation of H-Mordenite, 5-Mo/Mor, 10-Mo/Mor, and 15-Mo/Mor catalyst

Wavenumber (cm^{-1})				Bond type and vibration	Reference
H-mordenite	5-Mo/Mor	10-Mo/Mor	15-Mo/Mor		
455	455	455	455	Si-O/Al-O (Bending)	[26]
-	-	-	575	Mo-O	[28]
-	870	870	-	Mo-O-Mo (Stretching)	[28]
1640	1640	1640	1640	H-O-H (Bending)	[27]
3425	3425	3425	3425	Si-O-H (Stretching)	[26]

3.3. Catalyst crystallinity characterization using XRD

Catalyst crystallinity characterization result was shown in Figure 2 and Table 3. Based on the diffractogram as shown in Figure 2, H-mordenite, 5-Mo/Mor, 10-Mo/Mor, and 15-Mo/Mor catalysts had several sharp peaks and tended to be consistent. A diffraction pattern that has a peak characterization with high intensity or a sharp peak is a material with a crystalline structure [30]. This statement is reinforced by analyzing the degree of crystallinity for each catalyst sample in Table 3 using Origin Pro software by dividing the amount of crystalline peak area by the total area in each diffractogram. Mo metal loading causes a decrease in the degree of crystallinity of the catalyst. This occurs since, when a metal is loaded into a pore, there will be changes in the interaction between the surface of the pore and the metal [31]. As a consequence, many sharp peaks did not appear on the diffractogram of the metal-embedded catalyst variation compared to the diffractogram of mordenite.

The analysis of the mineral content of the catalyst was carried out by comparing the data of inter-plane distance and diffraction angle value (2θ) with the database of JCPDS (Joint Committee on Powder Diffraction Standard), which was important to know what compounds were contained in the catalyst sample. The results of the XRD analysis provided X-ray diffractogram peaks with a match with the JCPDS database for the mineral mordenite. With JCPDS card no. 006-0239, the 5-Mo/Mor catalyst showed crystal peaks at 23.6, 25.7, 27.4, and 27.7°, which are the characteristic peaks of MoO_3 (JCPDS card no. 005-0508), 10-Mo/Mor that showed crystal peaks at 12.8, 23.2, 25.8, 27.2, and 33.7° as the characteristic peaks of MoO_3 (JCPDS card no. 005-0508), and 15-Mo/Mor catalyst shows crystal peaks at 25.8, 36.9, 37.3, and 53.3° as the characteristic peaks of MoO_2 (JCPDS card no. 032-0671). This indicated that the 5-Mo/Mor, 10-Mo/Mor, and 15-Mo/Mor catalysts used in this study were the mordenite minerals and impregnated by Mo metal. Despite the impregnation, the Mo was still in oxide forms. This might be caused by the reduction process that required need higher temperature, longer time, or gas flow.

3.4. Catalyst morphology and composition characterization using SEM-EDX

Catalyst morphology and composition by SEM-EDX was shown in Figure 3, Table 4, and Figure 4. Figure 3 shows that

the surface of the mordenite catalyst tended to be hollow lumps with the uneven surfaces. The 5-Mo/Mor, 10-Mo/Mor, and 15-Mo/Mor catalyst SEM images show that the metal-impregnated mordenite Mo had larger particles compared to the particles of mordenite. The presence of these particles indicated metal impregnation on the catalyst surface. Based on the SEM image of 10-Mo/Mor catalyst, the higher the metal concentration variation, the larger and more particles are visible, thus giving a slight change in morphological shape compared to before the metal impregnation process was carried out. In addition, there are also many cavities on the surface of the catalyst. This indicated an opening of new pores at the active site of the catalyst due to the addition of Mo metal

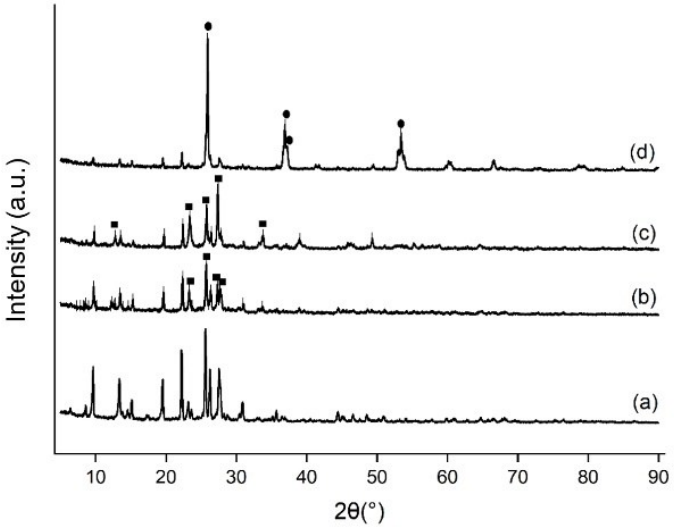

Fig. 2 Diffractogram of: (a) H-mordenite (b) 5-Mo/Mor; (c) 10-Mo/Mor; and (d) 15-Mo/Mor catalyst using XRD

Table 3. Degree of crystallinity of H-Mordenite, 5-Mo/Mor, 10-Mo/Mor, and 15-Mo/Mor catalyst

Sample	Degree of crystallinity (%)
H-mordenite	55.55
5-Mo/Mor	49.71
10-Mo/Mor	41.07
15-Mo/Mor	31.10

.

Based on the EDX result in Table 4, Mo metal was successfully impregnated into mordenite with the appearance of Mo composition in the catalyst variation. However, there was a difference between the Mo value measured on the instrument and the theoretical value. The 5-Mo/Mor, 10-Mo/Mor, and 15-Mo/Mor catalysts theoretically had Mo contents of 5, 10, and 15%, respectively. While, the EDX analysis results showed that the Mo value impregnated was different from the theoretical value. The elemental mass calculation method in SEM-EDX does not apply to the entire sample being analyzed but only to certain surface points. Thus, SEM-EDX could not provide information on the composition of the elements as contained in the entire sample. However, from the EDX results, the increasing trend of Mo metal composition was directly proportional to the theoretical value of the increase in the variation of Mo metal.

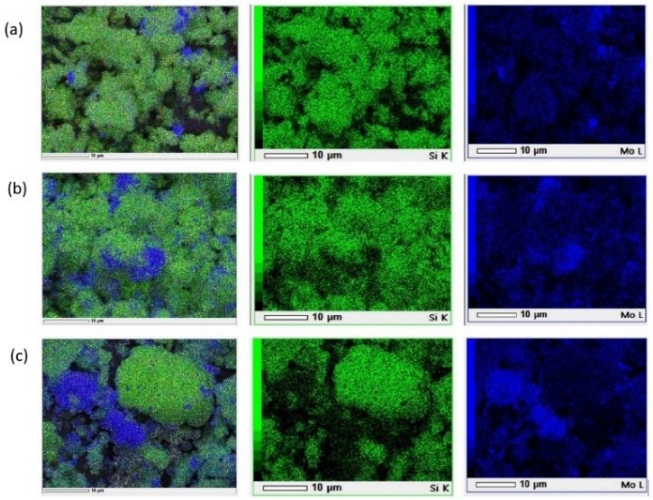

Fig. 3. SEM image of: (a) H-Mordenite; (b) 5-Mo/Mor; (c) 10-Mo/Mor; (d) 15-Mo/Mor catalyst

Table 4. Elemental composition of H-Mordenite, 5-Mo/Mor, 10-Mo/Mor, and 15-Mo/Mor catalyst

Sample	Composition (wt%)				
	C	Si	Al	O	Mo
Mordenite	10.69	28.06	3.41	47.04	-
5-Mo/Mor	8.16	26.23	3.20	52.18	4.65
10-Mo/Mor	8.35	29.54	3.37	47.39	6.25
15-Mo/Mor	3.01	24.15	2.98	45.52	24.34

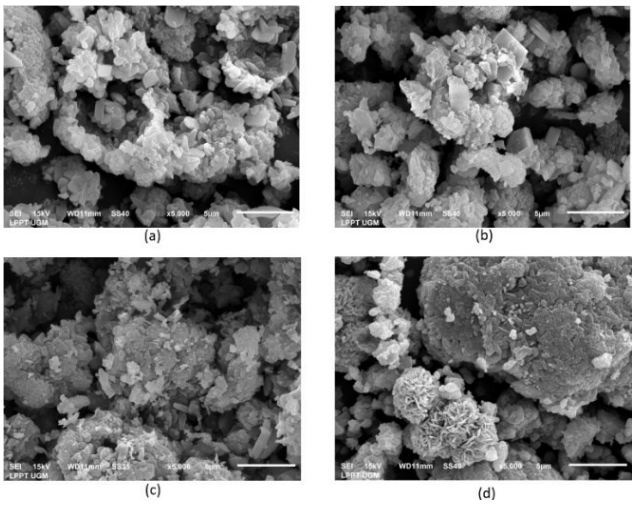

Fig. 4. Si and Mo distribution of: (a) 5-Mo/Mor; (b) 10-Mo/Mor; (c) 15-Mo/Mor catalyst using SEM-EDX mapping

The distribution of Mo elements on 15-Mo/Mor was found higher than that of on 5-Mo/Mor and 10-Mo/Mor in Figure 4. In addition, the distribution of Mo elements in 15-Mo/Mor formed agglomeration following the morphology of the catalyst. This distribution also indicated that Mo metal has been successfully embedded on the catalyst surface.

3.5. Catalyst textural characterization by nitrogen desorption with Brunauer-Emmett-Teller (BET) and Barrett-Joyner-Teller (BJH) equation

Table 5 presents the catalyst textural characterization result by nitrogen desorption with Brunauer-Emmett-Teller (BET)

and Barrett-Joyner-Teller (BJH) equation. The table shows a decrease in the surface area of metal-impregnated mordenite compared to the surface area of mordenite itself. This could be due to the addition of Mo metal, which caused agglomeration in the pores of the support so that the surface area of the catalyst was smaller than the specific surface area of mordenite. The surface area of 10-Mo/Mor and 15-Mo/Mor was larger than 5-Mo/Mor due to the larger amount of metal added. As a result, the metal did not only go on the pores of the carrier but also partially attached to the surface of the catalyst. The average pore diameter of 5-Mo/Mor, 10-Mo/Mor, and 15-Mo/Mor catalysts tended to increase compared to the average pore diameter of mordenite.

Table 5. Surface characterization of H-Mordenite, 5-Mo/Mor, 10-Mo/Mor, and 15-Mo/Mor

Sample	Surface area ($m^2 g^{-1}$)	Total pore volume ($cm^3 g^{-1}$)	Average pore diameter (nm)
H-Mordenite	394.06	0.22	2.23
5-Mo/Mor	59.81	0.05	3.27
10-Mo/Mor	111.41	0.08	2.81
15-Mo/Mor	164.55	0.02	4.55

3.6. Catalyst acidity using NH_3-TPD

Figure 5 and Table 6 show the catalyst acidity characterization result. Analysis curve in Figure 5 H-mordenite, 5-Mo/Mor, 10-Mo/Mor, and 15-Mo/Mor catalysts had three desorption peaks in Figure 5. Table 5 provides a summary of the total acidity of each catalyst. Based on the desorption temperature, the NH3-TPD acid site is classified as weak if the peak appears at a temperature of 120-300°C, moderate at a temperature of 300-500°C and strong at temperatures above 500°C [32]. The appearance of the peak of each catalyst at temperatures above 500°C indicates an increase in the acid site of the catalyst. Since weak acid sites had low interaction strength, it was difficult to engage with the acid sites of the catalyst during a reaction. Medium acid sites have moderate contacts and can interact with a reactant and then release it once the reaction is complete. Strong acid sites are so strong in interacting with the reactant and tend to react with fewer reactants due to harder reactant release after the reaction.

After Mo tal impregnation of, 5-Mo/Mor and 10-Mo/Mor had higher medium acid sites and total acidity. Mo metal has Brønsted acid function that increases acidity by intensifying the release of H+ protons. Meanwhile, 15-Mo/Mor had a decrease in total acidity and each acid site. The inefficient active sites with decreased specific surface area are caused by Mo metal clumping and agglomeration, as depicted in Figure 3 and 4.

Table 6. Acidity of H-Mordenite, 5-Mo/Mor, 10-Mo/Mor, and 15-Mo/Mor catalyst using NH_3-TPD

Sample	Acidity (mmol g^{-1})			Total acidity (mmol g^{-1})
	Weak acid site	Medium acid site	Strong acid site	
H-Mordenite	5.48	5.66	0.71	11.87
5-Mo/Mor	6.96	7.64	1.26	15.86
10-Mo/Mor	3.62	6.30	6.42	16.34
15-Mo/Mor	2.94	4.02	1.13	8.27

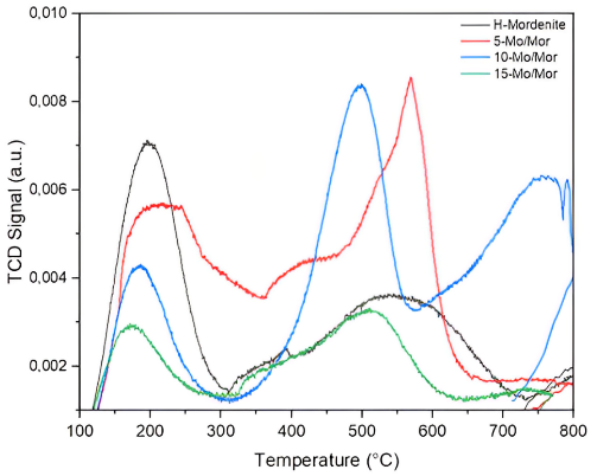

Fig. 5. NH_3-TPD analysis curve of H-Mordenite, 5-Mo/Mor, 10-Mo/Mor, and 15-Mo/Mor catalyst

3.7. Catalytic activity test

The catalytic activity test of RPKO hydrodeoxygenation result was shown in Table 7 and 8. As shown in Table 7, the liquid product of metal-impregnated mordenite catalyst had more liquid product than mordenite catalyst and thermal cracking results. Bioavtur was produced due to hydrogen was introduced to the fatty acid molecules during the hydrodeoxygenation process, whereas oxygen atoms were eliminated as water (H_2O). Bioavtur was converted from RPKO by hydrogenating the carbon chains to eliminate oxygen functions and saturate them. As Laurate acid is already in bioavtur range, there was no hydrocracking process. This might be due to the presence of metal in the catalyst, which would increase the catalytic properties of the catalyst. Hence, the liquid product produced was higher. Mo metal had a half-filled *d* orbital functioned as a Brønsted acid, which acted by encouraging the protonation of oxygen atoms. Brønsted acids improves the hydrodeoxygenation as catalyst active sites and makes it easier to remove oxygen later during the catalytic conversion process in the form of water leading to more HDO reaction and liquid product yield compared to thermal cracking as shown in Table 7. However, in the Mo/Mor catalysts, Mo oxide and had different configuration compared to Mo, but still provided the good results due to the ability to catalyze the HDO processes. The catalyst surface containing molybdenum species has made it easier for oxygen-carbon bonds in oxygenated organic molecules to break. The 15-Mo/Mor catalyst produces the most liquid products. The compounds

Table 7. Catalytic selectivity of RPKO hydrodeoxygenation using: Thermal cracking, H-Mordenite, 5-Mo/Mor, 10-Mo/Mor, and 15-Mo/Mor

Catalyst	Yield (wt%)			
	Liquid	Bioavtur	Non-bioavtur	Oxygenated compounds
Thermal Cracking	38.99	34.91	1.31	2.77
H-Mordenite	40.74	37.22	1.31	1.97
5-Mo/Mor	42.26	37.94	0.37	4.39
10-Mo/Mor	45.20	42.88	0.29	2.32
15-Mo/Mor	46.08	43.19	1.04	2.89

Table 8. Compounds distribution of liquid product from HDO using 15-Mo/Mor Catalyst

Retention time	Compound		Yield (wt%)		
	Name	Formula	400-500°C	500-600°C	Total
3.68 - 5.72	1-Heptene	C_7H_{14}	0.45	0.78	1.23
	n-Heptane*	C_7H_{16}	0.00	0.11	0.11
	4-Methylcyclohexene	C_7H_{12}	0.00	0.09	0.09
	Toluene*	C_7H_8	0.00	1.01	1.01
6.60 - 9.63	1-Octene	C_8H_{16}	0.97	1.05	2.02
	Octane*	C_8H_{18}	0.92	0.17	1.09
	Ethylbenzene	C_8H_{10}	0.00	0.09	0.09
	o-Xylene*	C_8H_{10}	0.00	0.16	0.16
10.61 - 13.19	1-Nonene	C_9H_{18}	1.69	1.37	3.06
	Nonane*	C_9H_{20}	1.93	0.30	2.23
	2-Nonene	C_9H_{18}	0.08	0.00	0.08
	4-Nonuna	C_9H_{16}	0.07	0.00	0.07
	2,4-Nonadiene	C_9H_{16}	0.09	0.00	0.09
14.60 - 16.99	1-Decene	$C_{10}H_{20}$	2.79	3.01	5.8
	n-Decane*	$C_{10}H_{22}$	1.28	0.38	1.66
	2-Decene	$C_{10}H_{20}$	0.32	0.00	0.32
	3-Isobutyl-1-cyclohexene	$C_{10}H_{18}$	0.07	0.08	0.15
18.25 - 18.96	1-Undecene	$C_{11}H_{22}$	3.07	3.07	6.14
	Undecane*	$C_{11}H_{24}$	6.71	2.11	8.82
	2-Decene	$C_{11}H_{22}$	0.12	0.31	0.43
21.29	2-Butyl-1-decene	$C_{14}H_{28}$	0.17	0.00	0.17
21.37	Naphthalene	$C_{10}H_8$	0.00	0.25	0.25
21.57 - 21.80	1-Dodecene	$C_{12}H_{24}$	0.00	1.61	1.61
	Dodecane*	$C_{12}H_{26}$	0.23	0.93	1.16
21.92	n-Tridecane*	$C_{13}H_{28}$	1.10	1.94	3.04
27.54 - 30.46	1-Tetradecene	$C_{14}H_{28}$	0.30	1.26	1.56
	Tetradecane*	$C_{14}H_{30}$	0.14	0.62	0.76
Total yield (wt%)			22.50	20.69	43.19
Total yield (wt%) main avtur compound				20.04	

Note * = Main avtur compound

contained in the reaction products are divided into bioavtur, non-bioavtur, and organic compounds. The bioavtur group is a hydrocarbon compound with carbon atoms numbered 7 to 16 (C_7–C_{16}), and the non-bioavtur group is a hydrocarbon compound excluded in the bioavtur range. The group of organic compounds is composed of saturated and unsaturated fatty acids that have not reacted completely, such as aldehydes, ketones, and alcohols. Table 7 shows that all catalysts were more selective towards the bioavtur fraction. The 15-Mo/Mor catalyst produced the highest bioavtur fraction of 43.19% as it had the largest surface area and highest Mo metal composition, so the catalyst made the most reaction. Table 8 shows compounds distribution that was contained in the liquid product from HDO of RPKO using 15-Mo/Mor catalyst.

Study conducted by Benavides et al. [33] stated that the hydrocarbon compound content of conventional aviation fuel samples had a distribution of the number of carbon atoms from C_7 to C_{19}, with the highest abundance owned by hydrocarbon compounds with the number of carbon atoms at 11. Table 8 shows that the HDO test using the 15-Mo/Mor catalyst produced a bioavtur yield containing the main aviation fuel compounds of 20.04wt% from the paraffin and aromatic compound groups in. Main avtur compound in 15-Mo/Mor bioavtur indicated potential. The compound distribution in Table 8 showed that the 15-Mo/Mor catalyst was the most selective catalyst for bioavtur products and produced the highest yield of main avtur compounds.

3.8. Comparison Between Studies of Catalyst Bioavtur Yield

Table 9 contains a comparison of the performance of 15-Mo/Mor catalyst with other studies. Date seed oil conversion to bioavtur using Pd-SiO_2 from waste glass and wet-impregnated by palladium chloride by Jrai et al. [34] produced 36.78wt% of bioavtur using autoclave batch reactor. Hassan et al. used Jatropha oil as feed and used activated Egyptian Bentonite B as catalyst [35]. Using a batch reactor at the high pressure of 78.9 atm, 40wt% of bioavtur was produced. Study by Carli et al. used NiMo and impregnated onto zeolite to convert oleic acid into bioavtur [36]. After 2.5 h in an autoclave batch reactor, 36.32wt% of bioavtur was produced. Multilevel reactor was used by Agaradathu et al. to produce bioavtur from the used cooking oil using NiMo-2/SiO_2 catalyst by dual metal co-impregnation with 2% of each Ni and Mo metal [37]. The bioavtur yield from the hydrocracking was 39.48%. Compared with those studies, the HDO reaction using a 15-Mo/Mor catalyst only used one type of metal but produced a higher bioavtur yield. Even, it did not use high pressure for the reaction resulting in less energy used during conversion. A study by Shetty et al. showing that the Mo metal had the characteristic suited for HDO reaction, especially in oxide forms [38]. The RPKO has a contribution to the higher bioavtur yield since it mostly consists of laurate acid, has 12 carbon chains, and is already in the bioavtur range. Thus, there is no need for the hydrocracking process. Therefore, Agaradathu et al. [37] and Carli et al. [36] also used Ni catalysts where Ni for hydrocracking and Mo for HDO. The RPKO conversion into bioavtur using 15-Mo/Mor catalyst used fewer materials and was more economical for bioavtur conversion.

Table 9. Catalyst performance on bioavtur production comparison with other studies

Catalyst	Feed	Reactor type	Condition	Bioavtur yield (wt%)	Reference
15-Mo/Mor	Palm kernel oil	Semi-batch with double furnace	300-600°C, H_2 gas flow of 10 ml min^{-1}, 4 h	43.19	Present work
Pd-SiO_2	Date seed oil	Autoclave batch	340°C, 150 rpm, 4 h	36.78	[34]
4% MB	Jatropha oil	Batch	350-450°C, 18 min, 78.9 atm	40.00	[35]
NiMo/Zeolit	Oleic acid	Autoclave batch	375°C, 1.48 atm, 2.5 h	36.32	[36]
NiMo-2/SiO_2	Used cooking oil	Multilevel	425°C, 1% catalyst-to-feed ratio, H_2 gas flow of 20 ml min^{-1}, 2 h	39.48	[37]

3.9. Usability test

The usability test of 15-Mo/Mor using HDO of RPKO feed was shown in Table 10 to 11, and Figure 6 to Figure 8. The 15-Mo/Mor catalyst had good stability for 3 times usage as shown in Table 8 and this can be seen from the resulting product in which the 15-Mo/Mor catalyst produced high liquid products even after 3 times usage. The second run produced a lower yield. Coke formation and Mo metal leaching from the catalyst affected the performance leading to lower Mo metal composition supported by the data in Table 9, resulting lower yield. The third run had a similar result to the first one and this showed a promising performance of bioavtur conversion that is not far from the fresh catalyst. This might be caused by Mo metal effective acid sites that were still active, distributed evenly and detected as shown in Figure 8 although covered by coke, only it had 4.29wt% composition, and the mordenite characteristic almost has gone as shown in Figure 6 and Figure 8.

After three runs, the 15-Mo/Mor catalyst morphology as shown in Figure 6 was covered in coke, leading the mordenite characteristic to almost go. The EDX analysis results in Table 11 showed a significant increase in C composition along with a decrease in Si, Al, O, and Mo composition after three runs. The temperature during the reaction did not contribute to the decrease of Si, Al, and Mo composition due to the melting point, but it was caused by the increase in C composition coming from the coke and hydrocarbon liquid products that stuck onto the catalyst resulting coke formation and metal leaching during the HDO run. The significant decrease in Si, Al, and O composition was caused by liquid product and coke formation, resulting in more C composition being detected and covering Si, Al, and O in Figure 7.

Table 10. Liquid product and bioavtur yield after 15-Mo/Mor usability test by HDO of RPKO feed.

Running	Yield (wt%)	
	Liquid	Bioavtur
1	46.08	43.19
2	34.82	32.58
3	46.14	43.45

Table 11. Elemental compositions of 15-Mo/Mor before and after usability test using EDX.

Catalyst	Composition (wt%)				
	C	Si	Al	O	Mo
15-Mo/Mor before usability test	3.01	24.15	2.98	45.52	24.34
15-Mo/Mor after usability test (3 HDO runs)	88.37	0.19	0.07	7.08	4.29

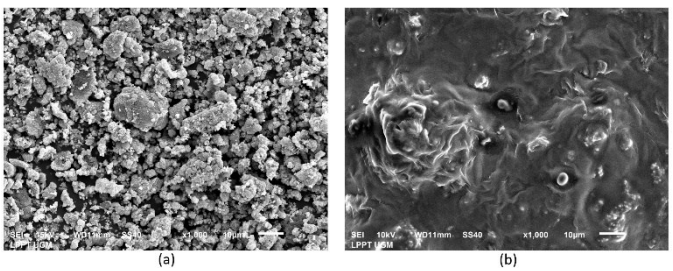

Fig. 6. SEM imaging of: (a) 15-Mo/Mor; (b) 15-Mo/Mor after 3 HDO runs.

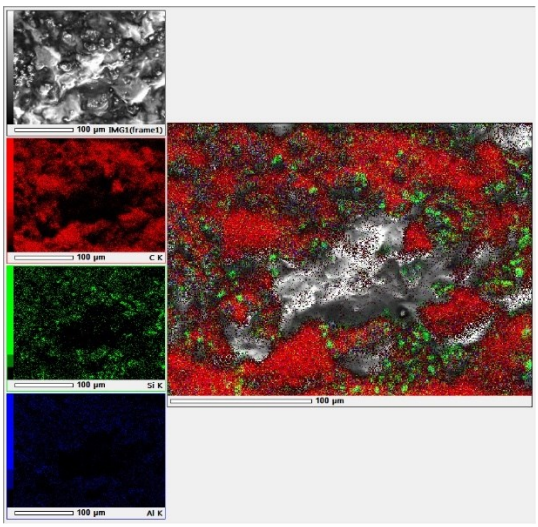

Fig. 7. Si and Al distribution of 15-Mo/Mor after 3 HDO runs using SEM-EDX Mapping.

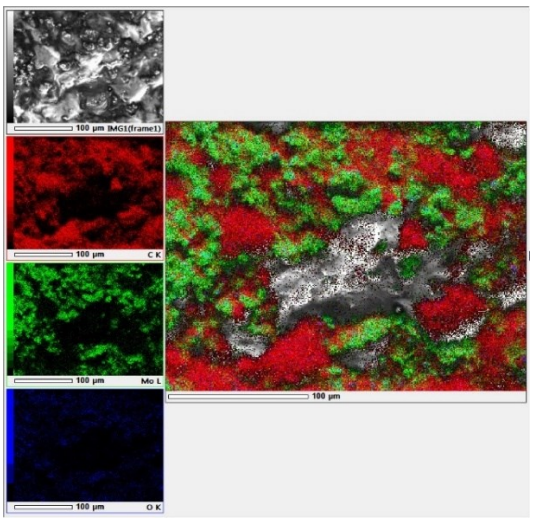

Fig. 8. Mo and O distribution of 15-Mo/Mor after 3 HDO runs using SEM-EDX Mapping.

4. Conclusion

The preparation of Mo/Mor catalysts with varying Mo metal content produced different characteristics. The surface area and pore diameter of the catalyst tended to increase as the Mo metal content increased, while the pore volume of the catalyst decreased as the Mo metal content increased. The 10-Mo/Mor catalyst had the highest total acidity value of 16.34 mmol g^{-1}, while the 5-Mo/Mor and 15-Mo/Mor catalysts had total acidity values of 15.86 and 8.17 mmol g^{-1}, respectively. In the activity and selectivity tests, the 5-Mo/Mor, 10-Mo/Mor, and 15-Mo/Mor catalysts produced the liquid products of 42.26, 45.20, and 46.08wt% with bioavtur compound contents of 37.94, 42.88, and 43.19wt%, respectively. The catalyst that produced the most liquid product and bioavtur, i.e. the 15-Mo/Mor catalyst, in the usability test showed good performance after three repeated HDO run. The liquid products produced in the second and third runs were 34.82 and 46.14wt%, with bioavtur fraction of 32.58 and 43.45wt%, respectively. The appearance of Mo oxides in the catalysts showed that future research need to develop better

impregnation method and adequate reduction process for more Mo bonding and completely reduced the Mo into Mo(0).

5. Acknowledgements

Sawit Grant BPDPKS with grant numbers PRJ-365/DPKS/2022 and 3660/UN1/DITLIT/Dit-Lit/PT.01.03/2022 provided funding for this study.

References

1. J. He et al., *Towards carbon neutrality: A study on China's long-term low-carbon transition pathways and strategies*, Environ. Sci. Ecotechnology. 9 (2022) 100134.
2. A. Scuderi, M. Cammarata, F. Branca, and G. Timpanaro, *Agricultural production trends towards carbon neutrality in response to the EU 2030 Green deal: Economic and environmental analysis in horticulture*, Agric. Econ. 67 (2021).
3. A. Raihan, *The contribution of economic development, renewable energy, technical advancements, and forestry to Uruguay's objective of becoming carbon neutral by 2030*, Carbon Res. 2 (2023).
4. G.K. Ayetor, A.K. Sunnu, and M.A. Kesse, *Engine performance and emissions of fuel produced from palm kernel oil*, Biofuels. 13 (2022).
5. J. Wang, et al., *Creating values from wastes: Producing biofuels from waste cooking oil via a tandem vapor-phase hydrotreating process, Appl. Energy* 323 (2022).
6. E. Kwao-Boateng, M. Agbedam, A.N.P. Agyemang, E. Acquah, K.A. Ofori, and A.T. Tagoe, *Comparative analysis of palm kernel and waste cooking oils for biodiesel production as an alternative fuel to conventional diesel fuel*, J. Ghana Inst. Eng. 23 (2023).
7. H. Wijayanti et al., *Evaluation of stirring rate and pH on phenolic compounds recovery from palm kernel shell heavy phase bio-oil*, Commun. Sci. Technol. 8 (2023).
8. R. Jelita, J. Jefriadi, M.J. Mahdi, and M. Hafiz, *Effect of temperature and blending ratio to product distribution of co-pyrolysis lignite and palm kernel shell*, Konversi 10 (2021).
9. J. Silalahi, L.K. Karo, S.M. Sinaga, and Y.C.E. Silalahi, *Composition of Fatty Acid and Identification of Lauric Acid Position in Coconut and Palm Kernel Oils*, Indones. J. Pharm. Clin. Res. 1 (2018) 1–8.
10. M. Makcharoen, A. Kaewchada, N. Akkarawatkhoosith, and A. Jaree, *Biojet fuel production via deoxygenation of crude palm kernel oil using Pt/C as catalyst in a continuous fixed bed reactor,* Energy Convers. Manag. X. 12 (2021) 100125.
11. A. Mancini, E. Imperlini, E. Nigro, C. Montagnese, A. Daniele, S. Orrù, and P. Buono, *Biological and nutritional properties of palm oil and palmitic acid: Effects on health*, Molecules. 20 (2015) 17339–17361.
12. R. El-Araby, E. Abdelkader, G. El Diwani, and S.I. Hawash, *Bio-aviation fuel via catalytic hydrocracking of waste cooking oils*, Bull. Natl. Res. Cent. 44 (2020) 1.
13. D. Guo, B. Cai, R. Kang, S. Wang, J. Feng, and H. Pan, *Selective hydrodeoxygenation of guaiacol to cyclohexanol over NixCoyAlz catalysts under mild conditions*, J. Anal. Appl. Pyrolysis 170 (2023) 105876.
14. P. Wang et al., *Highly efficient alloyed NiCu/Nb_2O_5 catalyst for the hydrodeoxygenation of biofuel precursors into liquid alkanes*, Catal. Sci. Technol. 10 (2020).
15. H. Xu and H. Li, *Alcohol-assisted hydrodeoxygenation as a sustainable and cost-effective pathway for biomass derivatives upgrading*, J. Energy Chem. 73 (2022) 133–159.
16. T. Dickerson and J. Soria, *Catalytic fast pyrolysis: A review*, Energies. 6 (2013) 514–538.
17. E.W Qian, N. Chen, and S. Gong, *Role of support in deoxygenation and isomerization of methyl stearate over nickel-molybdenum catalysts*, J. Mol. Catal. A Chem. 387 (2014) .
18. W. Wang, Y. Yang, H. Luo, H. Peng, B. He, and W. Liu, *Preparation of Ni(Co)-W-B amorphous catalysts for cyclopentanone hydrodeoxygenation*, Catal. Commun. 12 (2011) 1275–1279.
19. W. Trisunaryanti, I.I. Falah, D.R. Prihandini, and M.F. Marsuki, *Synthesis of ni/mesoporous silica-alumina using sidoarjo mud and bovine bone gelatin template for hydrocracking of waste lubricant*, Rasayan J. Chem. 12 (2019) 1523–1529.
20. J. Liao, et al., *New approach for bio-jet fuels production by hydrodeoxygenation of higher alcohols derived from C-C coupling of bio-ethanol*, Appl. Energy. 324 (2022) 119843.
21. C. Guild, S. Biswas, Y. Meng, T. Jafari, A.M. Gaffney, and S.L. Suib, *Perspectives of spray pyrolysis for facile synthesis of catalysts and thin films: An introduction and summary of recent directions*, Catal. Today. 238 (2014) 87–94.
22. S. Sriatun, H. Susanto, W. Widayat, and A. Darmawan, *Hydrocracking of coconut oil on the NiO/Silica-rich zeolite synthesized using a quaternary ammonium surfactant*, Indones. J. Chem. 21 (2021) 361–375.
23. M.S. Ibrahim, W. Trisunaryanti, and T. Triyono, *nickel supported parangtritis beach sand (pp) catalyst for hydrocracking of palm and malapari oil into biofuel*, BCREC 17(3) (2022).
24. I.K. Nugraheni, N. Nuryati, A.A.B. Persada, T. Triyono, and W. Trisunaryanti, *Impregnated zeolite as catalyst in esterification treatment from high free fatty acids palm oil mill effluent,* J. Rekayasa Kim. Lingkung. 16 (2021).
25. T. Triyono, W. Trisunaryanti, J. Purbonegoro, and S.I. Aksanti, *Effect of cobalt impregnation methods on Parangtritis sand towards catalysts activity in hydrocracking of degummed low-quality Ujung Kulon Malapari oil into biohydrocarbons*, React. Kinet. Mech. Catal. (2023).
26. M. Faisal, S. Suhartana, and P. Pardoyo, *Zeolit Alam Termodifikasi Logam Fe sebagai Adsorben Fosfat (PO_4^{3-}) pada Air Limbah,* J. Kim. Sains dan Apl. 18 (2015) 91–95.
27. M.C.D Dominic, P.M.S. Begum, R. Joseph, D. Joseph, P. Kumar, and E.P. Ayswarya, *Synthesis, characterization and application of rice husk nanosilica in natural rubber*, Int. J. Sci. Environ. Technol. 2 (2013) 1027-1035.
28. S.K. Sen et al., *Characterization and Antibacterial Activity Study of Hydrothermally Synthesized h-MoO_3 Nanorods and α-MoO_3 Nanoplates*, Bionanoscience. 9 (2019) 873–882.
29. K. Wijaya, A. Nadia, A. Dinana, A.F. Pratiwi, A.D. Tikoalu, and A.C. Wibowo, *Catalytic hydrocracking of fresh and waste frying oil over ni-and mo-based catalysts supported on sulfated silica for biogasoline production*, Catalysts. 11 (2021) 1–15.
30. N. Septiani, *Analisis Struktur Kristal Lithium Oksida dan Niobium Pentaoksida dengan XRD SNF2015-VII-29 SNF2015-VII-30, Prosiding Seminar Nasional Fisika, Jakarta, DKI Jakarta, Indonesia, 2015, pp. 29–32.*
31. X.F. Li, R. Prins, and J.A. van Bokhoven, *Synthesis and characterization of mesoporous mordenite,* J. Catal. 262 (2009) 257–265.
32. R.A. Febriansyar, T. Riyanto, I. Istadi, D.D. Anggoro, and B. Jongsomjit, *Bifunctional $CaCO_3$ / HY catalyst in the simultaneous cracking-deoxygenation of palm oil to diesel-range hydrocarbons*, Indones. J. Sci. Technol. 8 (2023) 281–306.
33. A. Benavides, P. Benjumea, F.B. Cortés, and M.A. Ruiz, *Chemical composition and low-temperature fluidity properties of jet fuels*, Processes. 9 (2021) 1–13.
34. A.A. Jrai, A.H. Al-Muhtaseb, F. Jamil, and M.T.Z. Myint, *Green*

hydrocarbons fuel production from agricultural waste biomass in the presence of a novel heterogeneous catalyst, Biomass Convers. Biorefinery. (2023).

35. S.H. Hassan, N.K. Attia, G.I. El Diwani, S.K. Amin, R.S. Ettouney, and M.A. El-Rifai, *Catalytic hydrocracking of jatropha oil over natural clay for bio-jet fuel production,* Sci. Rep. 13 (2023) 13419.
36. M.F. Carli, B.H. Susanto, and T.K. Habibie, *Sythesis of bioavture through hydrodeoxygenation and catalytic cracking from oleic acid using NiMo/Zeolit catalyst,* E3S Web Conf. 67 (2018) 02023.
37. R.H. Agharadatu, K. Wijaya, Prastyo, Wangsa, and W.C. Oh, *Application of mesoporous nimo/silica (NiMo/SiO2) as a catalyst in the hydrocracking of used cooking oil into jet fuel*, Silicon. (2023).
38. M. Shetty, K. Murugappan, T. Prasomsri, W.H., Green, and Y., Román-Leshkov, *Reactivity and stability investigation of supported molybdenum oxide catalysts for the hydrodeoxygenation (HDO) of m-cresol*, J. Catal. 331 (2015).